Gu *et al. Microstructures* 2024;4:2024060
DOI: 10.20517/microstructures.2024.05

Microstructures

Research Article

Open Access

Optimizing stress impedance and medium-range ordered structure in $Fe_{46.6}Mo_{8.7}Cr_{24.6}B_{9.5}C_{10}Si_{0.6}$ amorphous alloy through tailored annealing treatment

Yao Gu[1,#], Yiming Zhao[1,#], Jiacheng Ge[1], Longlong Fan[2], Sihan Zhang[1], He Zhu[1], Si Lan[1,3]

[1]Herbert Gleiter Institute of Nanoscience, School of Materials Science and Engineering, Nanjing University of Science and Technology, Nanjing 210094, Jiangsu, China.
[2]Beijing Synchrotron Radiation Facility, Institute of High Energy Physics, Chinese Academy of Sciences, Beijing 100049, China.
[3]Center for Neutron Scattering, City University of Hong Kong Shenzhen Research Institute, Shenzhen 518057, Guangdong, China.
[#]Authors contributed equally.

Correspondence to: Dr. He Zhu, Herbert Gleiter Institute of Nanoscience, School of Materials Science and Engineering, Nanjing University of Science and Technology, Lingxiaowei Road 200, Nanjing 210094, Jiangsu, China. E-mail: hezhu@njust.edu.cn; Dr. Si Lan, Herbert Gleiter Institute of Nanoscience, School of Materials Science and Engineering, Nanjing University of Science and Technology, Lingxiaowei Road 200, Nanjing 210094, Jiangsu, China; Center for Neutron Scattering, City University of Hong Kong Shenzhen Research Institute, Shenzhen 518057, Guangdong, China. E-mail: lansi@njust.edu.cn

How to cite this article: Gu Y, Zhao Y, Ge J, Fan L, Zhang S, Zhu H, Lan S. Optimizing stress impedance and medium-range ordered structure in $Fe_{46.6}Mo_{8.7}Cr_{24.6}B_{9.5}C_{10}Si_{0.6}$ amorphous alloy through tailored annealing treatment. *Microstructures* 2024;4:2024060. https://dx.doi.org/10.20517/microstructures.2024.05

Received: 15 Jan 2024 **First Decision:** 18 Mar 2024 **Revised:** 23 Mar 2024 **Accepted:** 29 May 2024 **Published:** 17 Oct 2024

Academic Editor: Zibin Chen **Copy Editor:** Fangling Lan **Production Editor:** Fangling Lan

Abstract

Amorphous alloys are emerging as a highly promising category of materials for mechanical sensing, attributed to their favorable stress impedance performance. However, the practical achievement of the stress impedance ratio still falls considerably short of its theoretical potential, and the atomic-scale mechanisms underlying this phenomenon remain largely unexplored. Here, we report that the stress impedance ratio of $Fe_{46.6}Mo_{8.7}Cr_{24.6}B_{9.5}C_{10}Si_{0.6}$ amorphous alloy can be significantly enhanced by a tailored annealing treatment around the glass transition temperature (T_g), giving rise to the highest stress impedance ratio reaching up to 124%. Utilizing the high-energy synchrotron X-ray total scattering technique, the strong correlation between the stress impedance performance and the medium-range ordered structure of amorphous alloys is elucidated. Our findings revealed that an increase in edge-sharing atomic connection mode plays a pivotal role in enhancing the stress impedance performance. Furthermore, a composite film combining the amorphous alloy with silicone rubber was fabricated under the same annealing treatment, demonstrating a significantly improved sensitivity compared to the ribbon (706.10 *vs.*

32.93 MPa^{-1}). This work not only contributes valuable insights into the atomic-scale mechanisms governing stress impedance in amorphous alloys but also proposes a general annealing strategy that holds the potential for unlocking new avenues in advanced sensing applications.

Keywords: Amorphous alloy, stress impedance effect, structural entropy, medium-range ordering, composite film

INTRODUCTION

Amorphous alloys have attracted considerable interest due to their unique physical and chemical properties compared to their crystalline counterparts. The inherent atomic disorder in these alloys eliminates magnetic domain structures, leading to an overall magnetic isotropy. This unique characteristic endows the majority of amorphous alloys to exhibit soft magnetic properties characterized by low coercivity, high permeability, and a high saturation magnetic flux density[1-6]. Furthermore, the soft magnetic features allow these amorphous alloys to exhibit a greater tendency for magnetic domain deflection under external forces. This, in turn, facilitates a more pronounced change in magnetic permeability, leading to high-sensitivity magnetoelastic coupling effects and a high stress impedance ratio. Therefore, the soft-magnetic amorphous alloys are becoming increasingly important in advanced sensor applications[7,8], surface coatings[9], and 3D printed components[10]. The stress impedance effect, referring to a significant impedance change under varying stress levels[11,12], establishes a link between applied stress and magnetostriction, emphasizing critical interplays of both mechanical and magnetic properties. Despite extensive engineering, the unexplored atomic-scale mechanism hinders the full potential and widespread adoption of stress impedance-based sensors.

So far, substantial efforts towards improving stress impedance properties have been made *via* various methods[13-18], wherein introducing nanocrystals to enhance structural anisotropy is an effective approach[19]. For example, a recent research work involved small bcc nanoclusters into the amorphous matrix, significantly enhancing the stress impedance and lowering local magnetic anisotropy. Another inspiring approach is to anneal the amorphous alloys at sub-T_g temperatures, where the T_g refers to glass transition temperatures. It has been found that annealing Fe-Dy-B-Nb amorphous at a temperature just below T_g, known as T_{AEP} annealing, increases stress impedance by about 30% compared to the as-cast state[20,21]. For this reason, Tong *et al.* revealed that annealing near T_g leads to improved magnetization and reduced coercivity, triggering evolution of short- and medium-range structures[22]. Here, short-range ordering (SRO) refers to atomic ordering within a range of 0-5 Å, while medium-range ordering (MRO) corresponds to a larger ordering range of 5-20 Å. However, at present, there remains a gap regarding the correlation between the short- to medium-range ordered structure in amorphous alloys and the stress impedance effect.

In this work, we improve the stress impedance ratio of $Fe_{46.6}Mo_{8.7}Cr_{24.6}B_{9.5}C_{10}Si_{0.6}$ amorphous alloy through a precisely tailored annealing treatment around T_g. Using high-energy synchrotron X-ray techniques, we establish a strong correlation between stress impedance and the medium-range ordered structure of the amorphous alloy. It has been revealed that the edge-sharing atomic connection mode plays a crucial role. Furthermore, a composite film combining the amorphous alloy with silicone rubber was made using the same annealing treatment, which exhibits a much better sensitivity. This research provides insights into atomic-scale mechanisms and suggests a promising annealing strategy for advanced sensing applications.

EXPERIMENTAL SECTION

Sample preparation

$Fe_{46.6}Mo_{8.7}Cr_{24.6}B_{9.5}C_{10}Si_{0.6}$ ingots were first prepared through vacuum induction melting using high-purity elements (> 99.95%). These ingots were then cast into dense, chemically homogeneous metal ingots through arc melting. Subsequently, the metal ingots were made into amorphous ribbons using a single roller melt spinning method. The thickness of the amorphous ribbons ranged from 10 to 0.02 μm, with a width between 1 and 1.4 mm. Before preparing the amorphous ribbons, the oxide layer on the surface of the metal ingots was removed using a grinding machine to ensure uniform nucleation.

The achieved $Fe_{46.6}Mo_{8.7}Cr_{24.6}B_{9.5}C_{10}Si_{0.6}$ amorphous ribbons were positioned within a round-bottom flask. This assembly was then evacuated using a vacuum sealing machine (model MRVS-1002) to achieve vacuum conditions. After sealing, the encapsulated materials were placed inside a muffle furnace (model MF-1200C-M, manufactured by BEQ) where they underwent heat treatment. The thermal processing was conducted at temperatures of 573, 823, 858, and 893 K, with a duration of 15 min for each temperature regime. The amorphous powders with a particle size ranging from 16 to 54 μm and identical composition were produced in collaboration with Guangzhou Wandun Non-Brand Trade Co., Ltd. by gas atomization. Amorphous powders were used to fabricate $Fe_{46.6}Mo_{8.7}Cr_{24.6}B_{9.5}C_{10}Si_{0.6}$/silicone rubber composite film. A miniature kneading machine (ZG-50D) blended the amorphous powders into silicone rubber at various mass fractions. To ensure particle uniformity, the powders were sieved with a 500-mesh sieve. During the kneading process, 2 wt% of reinforcing agent (white carbon black) and 2 wt% of vulcanizing agent (XH-C-2OH) were added into the mixture. The entire kneading process lasted for three hours to prevent the agglomeration of the amorphous powders in the silicone rubber matrix. After kneading, the roll gap of the kneading machine was adjusted to 0.4-0.5 mm to roll the uniformly mixed film. Finally, it was placed in a constant temperature air drying oven at 145 °C for 1 h to cure, resulting in the $Fe_{46.6}Mo_{8.7}Cr_{24.6}B_{9.5}C_{10}Si_{0.6}$/silicone rubber composite film.

Characterization

The crystal structures of the ribbons and powders were analyzed using X-ray diffraction (XRD, Bruker D8 Advance) with Cu Kα target (λ = 0.154 nm) operated at 40 kV. The morphology and composition were characterized using a scanning electron microscope (IT500HR SEM) equipped with X-ray energy dispersive spectroscopy (EDS). Differential scanning calorimetry (DSC) experiments were carried out using a Netzsch Pegasus DSC equipment under a high-purity Ar atmosphere, with a heating rate of 20 K min^{-1}. The mass of the test sample was about 30 mg.

Pair distribution function analysis

The synchrotron X-ray total scattering measurements were performed at the BL13SSW beamline of the Beijing Synchrotron Radiation Source (BSRF) (λ = 0.2061) using the transmission mode. The Q_{max} and Q_{min} values of S(Q) are 16.9 and 0.02 $Å^{-1}$, respectively. The background signal of the Kapton tape was subtracted from the raw data before the Fourier transform. The raw data were analyzed using the PDFgetX2 software to obtain the structure factor S(Q) ($Q = 4\pi\sin\theta/\lambda$, where θ is the scattering angle, and λ is the X-ray wavelength). The pair distribution function (PDF) G(r) was calculated *via* Fourier transform:

$$G(r) = \int_{Q\min}^{Q\max} (S(Q) - 1)Q\sin(Qr)dQ$$

where r is the distance of atom pairs, and Q_{max} is the maximum value of Q after Fourier transform. The peaks of $G(r)$ were fitted according to the exponential decay function $f(r) = A \times \exp(-r/\xi)$, where ξ describes the decay rate of the order. The G(r) was converted to the atomic PDF $g(r)$ using:

$$g(r) = \frac{G(r)}{4\pi r\rho_0} + 1$$

where ρ_0 is the average number density. The $g(r)$ was converted to structural entropy S_{eq} using S_{eq}=-$2\pi\rho_0 k_B\int(g(r)\ln g(r)-g(r)+1)r^2dr$[23], where k_B is the Boltzmann constant.

The first peak of $G(r)$ was transformed into $T(r)$ through the equation $T(r) = 4\pi r\rho_0 + G(r)$, where the $T(r)$ is believed to accord better with the Gaussian function than $g(r)$ and is more frequently employed to describe the SRO in amorphous alloys. The first $T(r)$ peak can be decomposed into the sum of the weighted Gaussian functions:

$$T(r) = \sum_i \sum_{J\le i} 4\pi r\rho_{ij}(r)\omega_{ij}$$

$\omega = 2c_ic_jb_ib_j/b^2$ (i ≠ j) or c_ib_i/b^2 (i = j)

$$b = \sum_i c_ib_i$$

where i and j are the ith and jth atomic species, ω_{ij} is the weight of the i-j pair, c_i (c_j) is the atom fraction, b_i (b_j) is the atom scattering factor, and b is the average scattering length. We calculated all the possible groups of atom pairs and found that Fe-(B, C), (Fe, Cr)-(Fe, Cr), and (Fe, Cr, Mo)-Mo share the largest weighted proportion. The theoretical bond lengths based on ionic radii were used as the initial input for the first Gaussian peak fitting. For the second peak fitting, the four polyhedron connection modes, i.e., 1-, 2-, 3- and 4-atom connections, were calculated to be 2R, √3R, √8/3R and√2R, respectively, according to the center-to-center distances of the four clusters.

Stress impedance performance testing

To measure the change in impedance (Z) in response to tensile stress (σ) of the amorphous ribbons at a frequency of 1 MHz, an impedance analyzer (LCR Meter IM3536, HIOKI) and a microcomputer-controlled electronic universal testing machine (UTM4304GD, SUNS) were employed. The entire testing process was carried out at room temperature. The stress-impedance ratio (SI) is defined as:

$$\mathrm{SI} = \frac{\Delta Z}{Z} = \frac{\left|z_{(\sigma)} - z_{(\sigma=0)}\right|}{z(\sigma = 0)}$$

where $Z(\sigma)$ is the impedance measured under tensile stress σ, and $Z(0)$ is the impedance measured without applying tensile stress σ.

Magnetic testing

A comprehensive physical property measurement system model, QYNACOOL-9 (QUANTUM DESIGN, Inc., USA), was used to measure the hysteresis loops of the amorphous alloys. A portion of the amorphous alloy ribbon with a size of about 2 mm × 3 mm was intercepted, weighed and attached to a sample rod and placed in a sample chamber, with helium gas as a protective gas. The Vibrating Sample Magnetometer (VSM) option was activated to select the appropriate program for the test. The hysteresis loop was measured with a constant temperature setting of 300 K and an applied magnetic field of 0-10,000 Oe.

The magnetostrictive property test system used in this work consists of an MTI-2000 fiber optic displacement measuring instrument (resolution up to 0.1 μm), a signal generator (Agilent 33500B, 1 μHz-80 MHz), a power amplifier (LYB-5040, output voltage ± 50 V, output current ± 12 A), a Helmholtz coil (generates magnetic field uniformly distributed area of 30 mm × 30 mm × 30 mm, conversion factor of 28 Oe A^{-1}), and a NI 9223 acquisition card. The tests were conducted using a signal generator to produce a sinusoidal signal with an amplitude of 1 V and a frequency of 1 Hz.

RESULTS AND DISCUSSION

Figure 1A provides the DSC curve of the $Fe_{46.6}Mo_{8.7}Cr_{24.6}B_{9.5}C_{10}Si_{0.6}$ ribbon. During the annealing process, the amorphous alloy gradually crystallizes, with the T_g at 833 K and the onset temperature of crystallization (T_x) at 893 K. The inset displays the XRD pattern of the amorphous ribbon, revealing a broad hump indicating the amorphous nature of the as-cast Fe-Cr-Mo-Si-B-C. Figure 1B shows the S(Q)s of the as-prepared and annealed samples at different temperatures. For the as-prepared sample, the S(Q) data shows a smooth feature without sharp crystallization peaks, further demonstrating the fully amorphous nature. Even after annealing at 828 K, the amorphous ribbon remains amorphous. The sharp crystallization peaks appear when annealing at 858 and 893 K, above T_g, consistent with the DSC results.

The above annealing treatment can eliminate the internal residual stress and tailor the atomic-scale structure of the amorphous alloy, which influences the magnetic domain structure and thereby enhances stress impedance performance[24-27] (discussed later). Figure 2A shows the stress impedance of Fe-Cr-Mo-Si-B-C ribbons annealed at variable temperatures. The stress impedance ratio increases with the annealing temperature increasing from 575 to 823 K, reaching up to about 124%. As the temperature further increases, the material experiences a decline in stress impedance ratio due to crystallization. Meanwhile, as shown in Figure 2B, the magnetization of the Fe-Cr-Mo-Si-B-C ribbon presents a similar temperature-dependent trend with the stress impedance ratio, exhibiting an initial increase followed by a subsequent decline with increasing temperature. The sample annealed at 823 K exhibits optimal soft magnetic performance. This demonstrates a close correlation between the stress impedance performance and soft magnetic properties of amorphous alloys, which could be derived from their atomic structures. As shown in Figure 2C, we explored the effect of annealing time on the stress impedance properties and the best stress impedance properties were measured for the amorphous strip annealed at 15 min. Figure 2D presents the magnetostriction for the ribbons annealed at varying temperatures. When lower magnetic fields (< 250 Oe) are applied, the magnetostrictions of the as-prepared and the 573K-treated samples are relatively strong, corresponding to higher stress impedance ratios under low stress for these two samples (see Figure 2A). However, at 300 Oe, the 823K-treated sample displays the strongest magnetostriction, consistent with the best stress impedance ratio at high stress.

To probe the atomic structure of the $Fe_{46.6}Mo_{8.7}Cr_{24.6}B_{9.5}C_{10}Si_{0.6}$ ribbons, high-energy synchrotron X-ray total scattering measurements were conducted. Figure 3A displays the PDF analysis of the total scattering data. The analysis of the decay trend of the PDF peak intensities was performed using the exponential decay function[28,29], as described in the Experimental Section. The simulated ξ values increase from 2.87 for the 573 K-treated sample to 3.34 for the 823 K-treated sample. This indicates that annealing the sample around T_g would enhance the degree of atomic ordering. For samples annealed at higher temperatures, the second PDF peak, corresponding to the MRO of the amorphous alloys, shows clear splits, which fingerprints a more ordered atomic structure in crystallized samples. In order to correlate atomic ordering in amorphous alloys with soft magnetic and stress impedance properties, the concept of structural entropy has been introduced (see Experimental Section). The structural entropy can be employed to systematically describe the SRO and MRO structures interconnected by the SRO units. As presented in Figure 3B, the structural

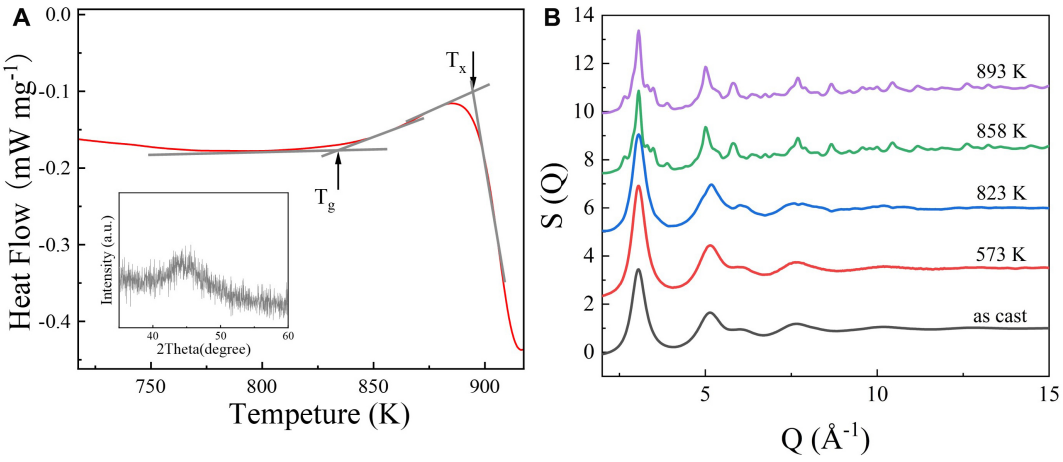

Figure 1. (A) DSC curve of $Fe_{46.6}Mo_{8.7}Cr_{24.5}B_{9.5}C_{10}Si_{0.6}$ amorphous alloy measured at a heating rate of 20 K·min^{-1}. The inset is the XRD pattern of the Fe-Cr-Mo-Si-B-C. (B) S(Q) curves of Fe-Cr-Mo-Si-B-C annealed at different temperatures.

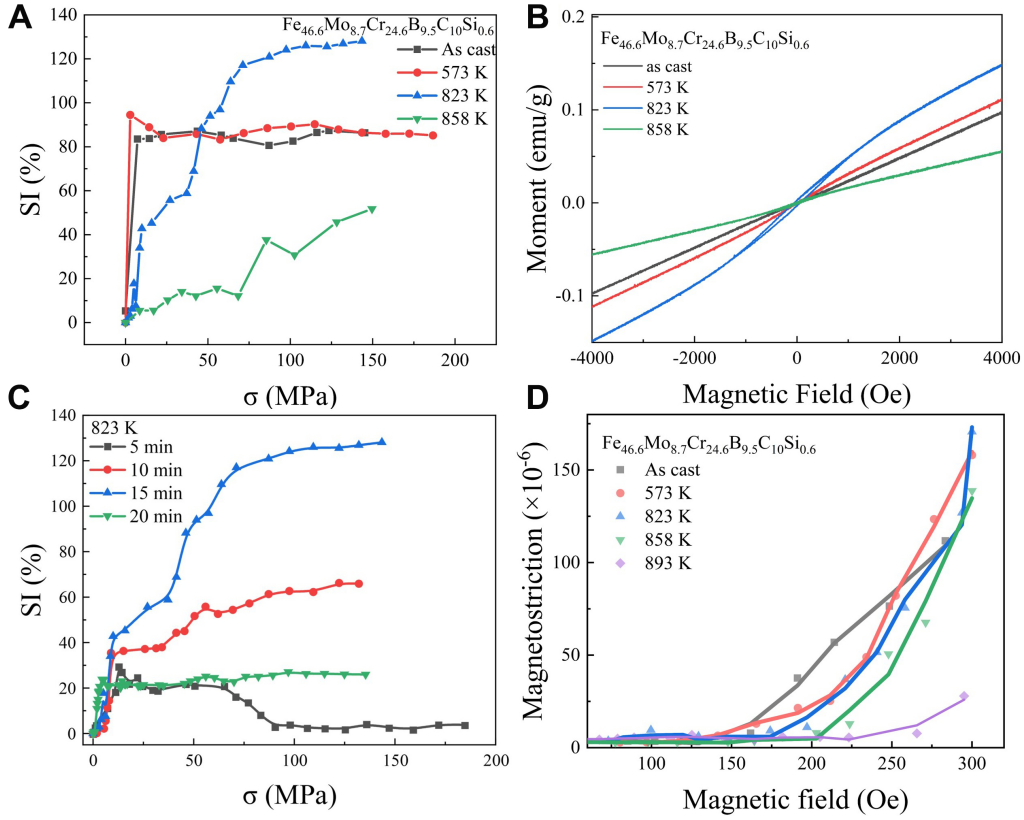

Figure 2. (A) Stress impedance performance and (B) soft magnetic properties of the as-prepared sample and those annealed at 573, 823, and 858 K, respectively. (C) Stress impedance performance of samples with different holding times at 823 K. (D) Magnetostriction of the as-prepared ribbon and those annealed at 573, 823, 858 and 893 K, respectively.

entropy phenomenon we obtained is consistent with phenomena in the previous literature[23]. The consistent variation of structural entropy and stress impedance with temperature further proves the strong correlation between atomic ordering and stress impedance performance in amorphous alloys.

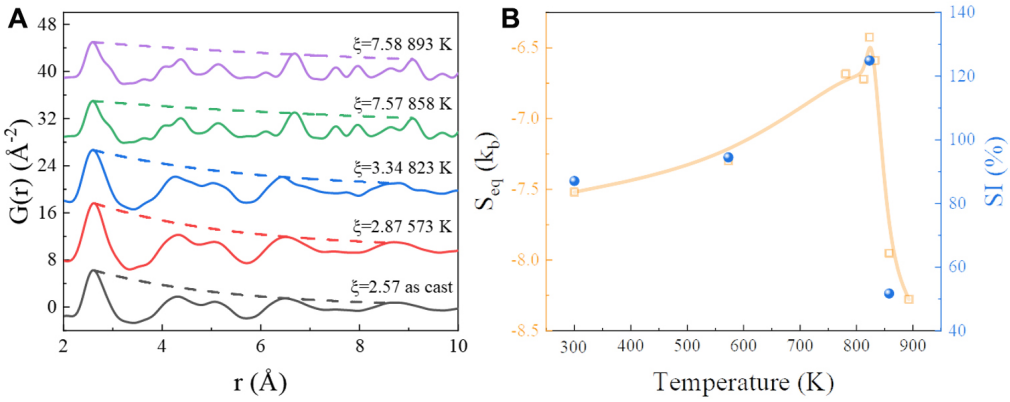

Figure 3. (A) Pair distribution function *G*(*r*) patterns analyzed by exponential decay function. (B) Relationship between structural entropy and stress impedance ratio at different temperatures.

When converting G(*r*) into atomic PDF g(*r*), the second g(*r*) peak at 3.5-5.5 Å corresponds to the MRO atomic clusters connected by SRO units, including point-shared (1-atom connection), edge-shared (2-atom connection), face-shared (3-atom connection), and embedded (4-atom connection) modes. Given the isotropic nature of amorphous alloys, a Gaussian function was used for fitting the second peak[30], as shown in Figure 4A-C. Cluster connectivity analysis reveals significant differences in atomic stacking after annealing treatments. Annealing treatment at T_g (i.e., 823 K) increases the proportion of edge-sharing modes and decreases the proportion of face-connecting modes, indicating the formation of uniform Fe-M (M refers to Si, B, P) atomic clusters. According to the solute-solute avoidance phenomenon[31,32], since the combination of Fe-M is more stable than M-M or Fe-Fe, there is a greater negative heat of mixing of Fe and M elements when annealing is performed at 823 K, which results in the formation of increasing homogeneous clusters of Fe-M atoms. In the medium-range order, the uniform Fe-M atomic clusters and the configuration stability of the residual matrix promote ferromagnetic exchange interactions[33]. These uniform Fe-M clusters weaken the heterogeneity of coupling energy, facilitating coherent movement and rotation of domain walls during the magnetoelastic coupling process, resulting in excellent response to applied stress[34,35]. Further annealing at higher temperatures reduces nanoscale heterogeneity, decreasing stress impedance performance. The PDF analysis reveals that the 823 K-annelaed sample exhibits the highest stress impedance ratio, confirming that the edge-sharing mode in MRO is beneficial for enhancing the stress impedance performance of amorphous alloys. When the temperature reaches 893 K, the proportion of edge-shared modes further increases, but the ribbon becomes fragile due to crystallization at this temperature, giving rise to a severe drop in the stress impedance ratio.

Figure 4D and E shows the fitting results of the first-shell peak for the as-prepared and 823 K-annealed samples, respectively. The amorphous ribbons annealed near T_g show a significant decrease in (Fe, Cr)-(Fe, Cr) and an increase in (Fe, Cr, Mo)-Mo in the first shell coordination. So, the annealing treatment also changes SRO, promoting magneto-electric conversion in amorphous alloys. The structural coordination in the short- and medium-range orders synergistically promotes the magnetic softening and stress impedance performance of the $Fe_{46.6}Mo_{8.7}Cr_{24.6}B_{9.5}C_{10}Si_{0.6}$ amorphous alloy. Further annealing at 893 K increases (Fe, Cr)-(Fe, Cr) and decreases (Fe, Cr, Mo)-Mo compared to 823 K [Figure 4F], accompanied with crystallization and fragility of the ribbon.

To validate the practical applicability of the high stress impedance performance of Fe-Mo-Cr-B-Si-C amorphous alloy, a composite film was fabricated by mechanically blending amorphous powders of the same composition with silicone rubber. Figure 5A presents the change of stress impedance ratio with the

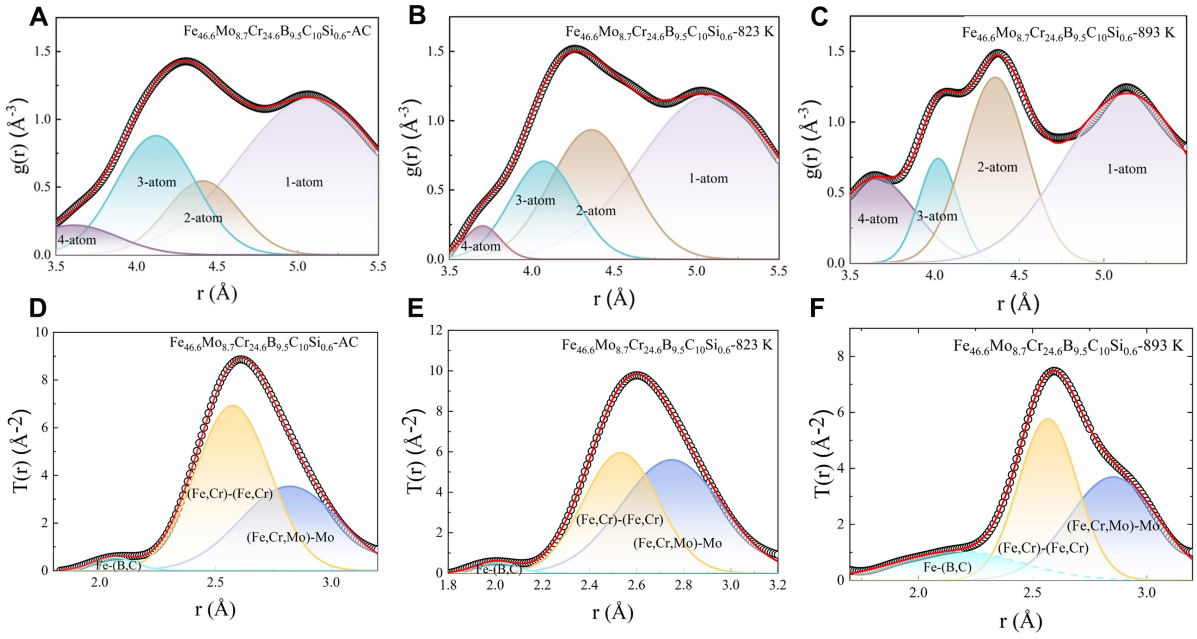

Figure 4. (A) Fitting results of different cluster connectivity modes in the second shell of as-prepared, (B) 823 K-annealed $Fe_{46.6}Mo_{8.7}Cr_{24.5}B_{9.5}C_{10}Si_{0.6}$ amorphous ribbons and (C) 893 K-annealed samples. (D) Fitting results of the first-shell T(*r*) peak of as-prepared, (E) 823 K-annealed samples and (F) 893 K-annealed samples.

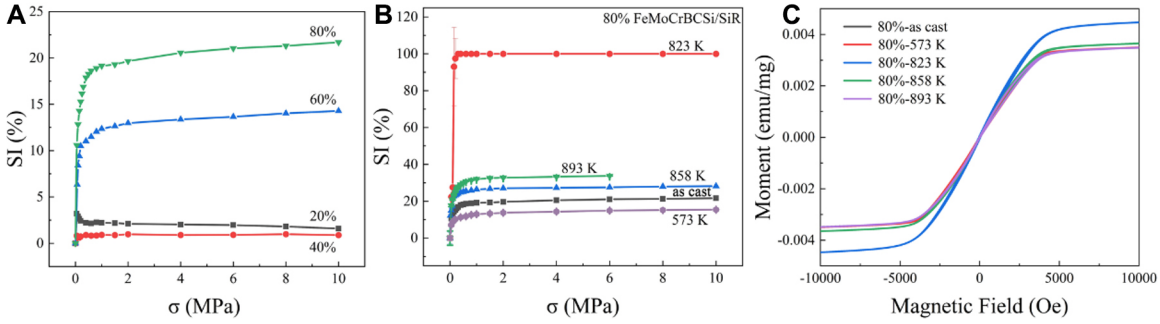

Figure 5. (A) Stress impedance performance of the composite films containing 20, 40, 60 and 80 wt% amorphous powders. (B) Stress impedance performance and (C) hysteresis loops of the composite films containing 80 wt% amorphous powders annealing at different temperatures.

content of as-cast amorphous powders in the composition film. As the powder content increases, the stress impedance ratio initially decreases and then rises, reaching its maximum value at a powder content of 80 wt%. When the powder content is higher than 80 wt%, the composite film cracks during the mechanical blending process due to the oversaturation of the powders in the silicone rubber. Therefore, we conducted annealing treatment, similar to that of ribbons, to the composite film containing 80 wt% powders. The changes in stress impedance performance are illustrated in Figure 5B. As expected, the composite film annealed at 823 K exhibits the highest stress impedance ratio compared to other temperatures, exhibiting a nearly 100% impedance change rate under 10 MPa [Figure 5C]. Remarkably, the sensitivity of the composite film, calculated by the slope of the impedance change rate, is much higher than that of the ribbons under the same annealing treatment (706.10 *vs.* 32.93 MPa^{-1}). This enhancement may be attributed to a faster response to mechanical stress enabled by the silicone rubber[36]. In addition, the magnetization loops of the composite films with 80 wt% powders were also determined under a maximum magnetic field of 10,000 Oe.

The 823 K-annealed sample shows the highest magnetization, consistent with its highest stress impedance ratio. Apart from the high sensitivity mentioned above, the combination of Fe-Mo-Cr-B-Si-C powders with silicone rubber also provides additional advantages such as flexibility, enhanced stability and durability, and improved noise resistance, which is promising for advanced mechanical sensor applications.

CONCLUSIONS

To summarize, our study demonstrates that the stress impedance performance of Fe-Cr-Mo-Si-B-C amorphous alloys could be enhanced by annealing treatment at the temperature around T_g. By high-energy synchrotron X-ray total scattering, we reveal a strong correlation between stress impedance performance and the medium-range ordered structure of amorphous alloys, specifically emphasizing the crucial role of increased edge-sharing atomic connection modes. Moreover, the successful fabrication of a composite film combining the amorphous alloy with silicone rubber under the same annealing treatment enables a remarkable improvement in sensitivity compared to traditional ribbons. This work proposes a general annealing strategy for preparing amorphous alloys with high stress impedance performance, which may promote the potential applications of amorphous alloys in advanced sensing technologies.

DECLARATIONS

Acknowledgment

Zhu H and Lan S acknowledge the support of the Beijing Synchrotron Radiation Facility.

Authors' contributions

Design: Lan S, Zhu H
Experiments and data collection: Gu Y, Zhao Y, Fan L, Zhang S
Data analysis: Gu Y, Zhao Y, Zhu H
Data analysis, manuscript writing: Ge J
Manuscript writing: Gu Y, Zhu H, Zhao Y
Manuscript revision and supervising: Lan S, Zhu H
All authors have read and agreed to the published version of the manuscript.

Availability of data and materials

The data that support the findings of this study are available from the corresponding author upon reasonable request.

Financial support and sponsorship

This study was financially supported by the National Key R&D Program of China (No. 2021YFB3802800), the National Natural Science Foundation of China (No. 52222104, No. 12261160364, and No. 22275089), and the Natural Science Foundation of Jiangsu Province (No. BK20200019). This research used the resources of high energy synchrotron radiation light source, Beijing Synchrotron Radiation Facility operated for Institute of High Energy Physics, Chinese Academy of Sciences.

Conflicts of interest

Lan S is an Editorial Board Member of the journal *Microstructures*. The other authors declare that there are no conflicts of interest.

Ethical approval and consent to participate

Not applicable.

Consent for publication

Not applicable.

REFERENCES

1. Mchenry ME, Willard MA, Laughlin DE. Amorphous and nanocrystalline materials for applications as soft magnets. *Prog Mater Sci* 1999;44:291-433. DOI
2. Deng S, Wang H, He L, Wang C. Magnetic structures and correlated physical properties in antiperovskites. *Microstructures* 2023;3:2023044. DOI
3. Zhao D, Chen Z, Liao X. Microstructural evolution and ferroelectricity in HfO_2 films. *Microstructures* 2022;2:2022007. DOI
4. Shen B, Inoue A, Chang C. Superhigh strength and good soft-magnetic properties of (Fe,Co)-B-Si-Nb bulk glassy alloys with high glass-forming ability. *Appl Phys Lett* 2004;85:4911-3. DOI
5. Inoue A, Shen B, Koshiba H, Kato H, Yavari AR. Cobalt-based bulk glassy alloy with ultrahigh strength and soft magnetic properties. *Nat Mater* 2003;2:661-3. DOI PubMed
6. Herzer G. Modern soft magnets: amorphous and nanocrystalline materials. *Acta Mater* 2013;61:718-34. DOI
7. Phan TA, Hara M, Oguchi H, Kuwano H. Current sensors using Fe-B-Nd-Nb magnetic metallic glass micro-cantilevers. *Microelectron Eng* 2015;135:28-31. DOI
8. Shen LP, Mohri K, Uchiyama T, Honkura Y. Sensitive acceleration sensor using amorphous wire SI element combined with CMOS IC multivibrator for environmental sensing. *IEEE Trans Magn* 2000;36:3667-9. DOI
9. Guo SF, Pan FS, Zhang HJ, et al. Fe-based amorphous coating for corrosion protection of magnesium alloy. *Mater Des* 2016;108:624-31. DOI
10. Huang S, Chen Q, Ji L, Wang K, Huang G. Microstructure and internal friction behavior of laser 3D printed Fe-based amorphous composites. *Acta Metall Sin* 2024;37:196-204. DOI
11. Bayri N, Atalay S. Giant stress-impedance effect in $Fe_{71}Cr_7Si_9B_{13}$ amorphous wires. *J Alloys Compd* 2004;381:245-9. DOI
12. Shen LP, Uchiyama T, Mohri K, Kita E, Bushida K. Sensitive stress-impedance micro sensor using amorphous magnetostrictive wire. *IEEE Trans Magn* 1997;33:3355-7. DOI
13. Suryanarayana C, Inoue A. Iron-based bulk metallic glasses. *Int Mater Rev* 2013;58:131-66. DOI
14. Huang B, Yang Y, Wang AD, Wang Q, Liu CT. Saturated magnetization and glass forming ability of soft magnetic Fe-based metallic glasses. *Intermetallics* 2017;84:74-81. DOI
15. Zhou XC, Chen SQ, Zhou MJ, Li M, Lan S, Feng T. Highly efficient cobalt-based amorphous catalyst for peroxymonosulfate activation toward wastewater remediation. *Rare Met* 2023;42:1160-74. DOI
16. Ketov SV, Sun YH, Nachum S, et al. Rejuvenation of metallic glasses by non-affine thermal strain. *Nature* 2015;524:200-3. DOI
17. Shuai S, Lu S, Xiang Z, Lu W. Stress-induced giant magneto-impedance effect of amorphous CoFeNiSiPB ribbon with magnetic field annealing. *J Magn Magn Mater* 2022;551:169131. DOI
18. Murali P, Ramamurty U. Embrittlement of a bulk metallic glass due to sub-T_g annealing. *Acta Mater* 2005;53:1467-78. DOI
19. Li X, Zhou J, Shen L, Sun B, Bai H, Wang W. Exceptionally high saturation magnetic flux density and ultralow coercivity via an amorphous-nanocrystalline transitional microstructure in an FeCo-based alloy. *Adv Mater* 2023;35:2205863. DOI
20. Ge JC, Liu AH, Wu ZD, et al. Phase transformation behavior of a dual-phase nanostructured Fe-Ni-B-Si-P-Nb metallic glass and its correlation with stress-impedance properties. *Rare Met* 2023;42:2757-66. DOI
21. Ge J, Gu Y, Yao Z, et al. Evolution of medium-range order and its correlation with magnetic nanodomains in Fe-Dy-B-Nb bulk metallic glasses. *J Mater Sci Technol* 2024;176:224-35. DOI
22. Tong X, Zhang Y, Wang Y, et al. Structural origin of magnetic softening in a Fe-based amorphous alloy upon annealing. *J Mater Sci Technol* 2022;96:233-40. DOI
23. Spieckermann F, Şopu D, Soprunyuk V, et al. Structure-dynamics relationships in cryogenically deformed bulk metallic glass. *Nat Commun* 2022;13:127. DOI PubMed PMC
24. Corte-León P, Zhukova V, Ipatov M, et al. High frequency giant magnetoimpedance effect of a stress-annealed Fe-rich glass-coated microwire. *J Alloys Compd* 2019;802:112-7. DOI
25. Corte-León P, Zhukova V, Ipatov M, Blanco JM, Zhukov A. Effect of Joule heating on giant magnetoimpedance effect and magnetic properties of Co-rich microwires. *J Alloys Compd* 2021;883:160778. DOI
26. Zhao C, Bruna P, Wang A, et al. Influence of magnetic field heat treatment on the microstructures and coercivity in ferromagnetic amorphous alloys. *J Mater Res Technol* 2022;21:4699-707. DOI
27. Lin J, Li X, Zhou S, et al. Effects of heat treatment in air on soft magnetic properties of FeCoSiBPC amorphous core. *J Non Cryst Solids* 2022;597:121932. DOI
28. Ma D, Stoica AD, Wang XL. Power-law scaling and fractal nature of medium-range order in metallic glasses. *Nat Mater* 2009;8:30-4. DOI PubMed

29. Lan S, Wu Z, Wei X, et al. Structure origin of a transition of classic-to-avalanche nucleation in Zr-Cu-Al bulk metallic glasses. *Acta Mater* 2018;149:108-18. DOI
30. Liu S, Wang L, Ge J, et al. Deformation-enhanced hierarchical multiscale structure heterogeneity in a Pd-Si bulk metallic glass. *Acta Mater* 2020;200:42-55. DOI
31. Dong BS, Zhou SX, Li DR, et al. Effects of solute-solute avoidance on metallic glass formation. *J Non Cryst Solids* 2012;358:2749-52. DOI
32. Sheng HW, Luo WK, Alamgir FM, Bai JM, Ma E. Atomic packing and short-to-medium-range order in metallic glasses. *Nature* 2006;439:419-25. DOI PubMed
33. Ouyang S, Song LJ, Liu YH, et al. Correlation between the viscoelastic heterogeneity and the domain wall motion of Fe-based metallic glass. *Phys Rev Mater* 2018;2:063601. DOI
34. Li Y, Shen N, Zhang S, et al. Crystallization behavior and soft magnetic properties of Fe-B-P-C-Cu ribbons with amorphous/α-Fe hierarchic structure. *Intermetallics* 2021;131:107100. DOI
35. Heo SI, Yun JC, Oh KS, Han KS. Influence of particle size and shape on electrical and mechanical properties of graphite reinforced conductive polymer composites for the bipolar plate of PEM fuel cells. *Adv Compos Mater* 2006;15:115-26. DOI
36. Zhou Y, Zhao X, Xu J, et al. Giant magnetoelastic effect in soft systems for bioelectronics. *Nat Mater* 2021;20:1670-6. DOI